Takeoff of a 2.1 g Fully Untethered Tailless Flapping-Wing Micro Aerial Vehicle With Integrated Battery

Takashi Ozaki ⬩, Norikazu Ohta, Tomohiko Jimbo ⬩, and Kanae Hamaguchi ⬩

Abstract—Insect-scale micro-aerial vehicles (MAV) are becoming increasingly important for sensing and mapping spatially constrained environments. However, achieving untethered flight powered by a small and lightweight on-board energy source remains a challenge. In this study, we successfully demonstrated the untethered takeoff of a flapping-wing MAV powered by a commercially available LiPo battery for a short duration without stability control. By incorporating a high-efficiency direct-drive piezoelectric actuator, and an optimized control circuit for high-impedance-width modulation and charge recovery, this electronics configuration realizes over 5 min of practical operation with a thrust of 1.5 times its own weight, while offering wireless communication capability and sensors for attitude estimation. Our MAV has a total mass of 2.1 g, which is an eight-fold reduction compared to the lightest battery-powered tailless flapping-wing MAV currently available, making this the first report of a battery-powered tailless flapping-wing MAV with insect-scale weight.

Index Terms—Aerial systems: mechanics and control, biologically-inspired robots, biomimetics.

I. INTRODUCTION

INSECT-SCALE micro-aerial vehicles (MAV) are useful for surveying, monitoring, and sensing applications in areas that are inaccessible to conventional multirotor drones and in situations where the use of larger drones poses a safety risk to people. One of the biggest technical challenges for ultra-compact MAVs is the lack of compact and lightweight energy sources at this scale. For example, the controlled flight of extremely small insect-like robots weighing less than 1 g has been realized without internal batteries [1], [2], [3], [4]. Reducing the total mass of battery-powered flight vehicles is difficult. A 28.2 g electromagnetic motor-driven tailless aircraft, powered by a battery, that can move freely in all directions and hover was first demonstrated [5]. Eventually, the total mass of this tailless flapping wing design was reduced to 19.7 g [6]. Similarly, other

research groups have reported controlled flights with motor-driven tailless aircraft weighing 21 g and 16.6 g [7], [8]. MAVs weighing 10 g or less have been reported such as those with a limited flight degree-of-freedom (DoF) using lift-by-forward flight [9], [10] while others have insufficient actuation DoFs required for flight control (e.g., having only one propulsion source for a demonstration of vertical takeoff) [11], [12]. In other words, realizing aircraft with insect-scale mass (a few grams to subgram), an internal battery, and configured with sufficient DoFs for flight control remains difficult.

Wireless power transmission technologies have been studied as an alternative to batteries. Insect-inspired subgram robots that use lasers and white light as energy sources have been demonstrated [13], [14]. Similarly, the successful takeoff of a 1.8 g aircraft using electromagnetic waves as an energy source has been reported [15]. However, both light and electromagnetic waves can be blocked by obstacles; therefore, for practical use, having at least a backup battery onboard to power the MAV so that it can move to a location where it can receive wireless power again is desirable.

In this study, we integrated a small LiPo battery, power conditioning circuit, microcontroller, and Bluetooth communication antenna into a piezoelectric-driven flapping winged aircraft we designed previously [15]. We then successfully demonstrated its untethered takeoff without attitude control. A new electronic circuit was designed to drive the piezoelectric elements with high energy efficiency, and the aircraft has a practical flight duration of more than 5 min. Our MAV is up to eight times lighter than any other state-of-the-art battery-powered tailless flapping MAV, making it the lightest battery-powered MAV to date [8]. This is also the first example of a piezoelectric-driven tailless aircraft with integrated batteries. In this letter, the comprehensive vehicle design and electronic components are presented in Section II. Section III is dedicated to the examination of the actuation performance of the MAV, illustrating the influence of our developed electronics, and includes a take-off demonstration of the vehicle. A summary of the findings and discussion of future research objectives are provided in Section IV.

II. DESIGN

A. Vehicle Overview

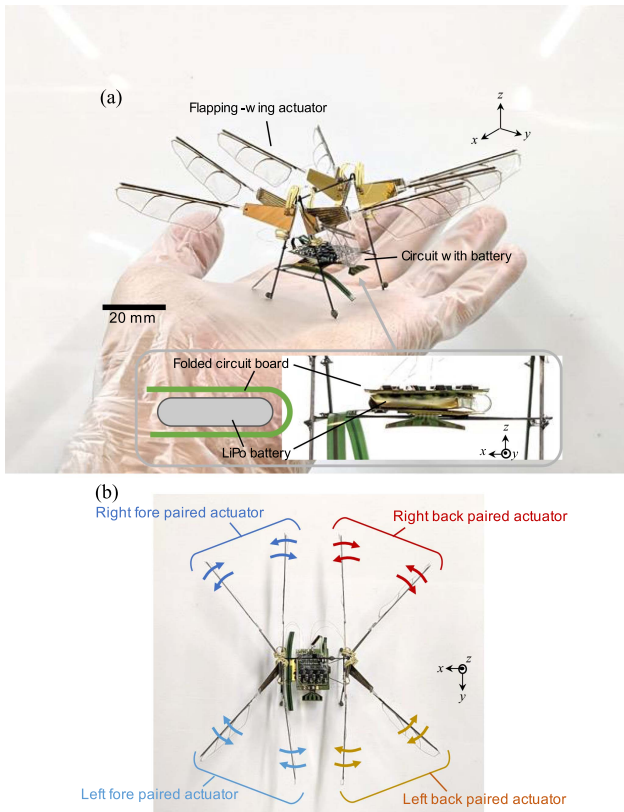Fig. 1 shows photographs of the fabricated MAV. The MAV is equipped with eight piezoelectric unimorph actuators and wings

Fig. 1. Battery-integrated flapping-wing MAV. (a) Photograph of fabricated MAV. (b) Configuration of flapping-wing actuators.

TABLE I
MASS DISTRIBUTION OF FABRICATED VEHICLE

Components		Mass (mg)
Vehicle without battery & circuit	Wings	143
	Unimorph actuators	928
	Body	198
	Adhesive*	39
	Total	1308
Battery		386
Circuit board		360
Adhesive & solder*		85
Total		2139

* The masses of adhesive and solder are derived by subtracting the mass of the components from the total mass.

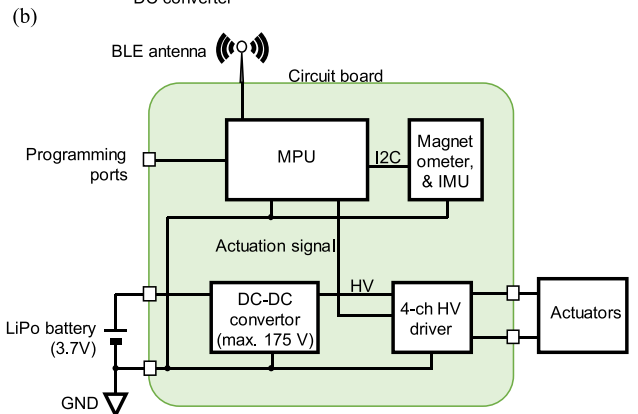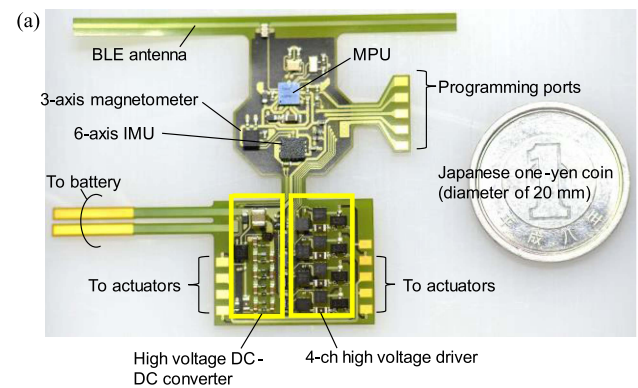Fig. 2. Lightweight flight electronics. (a) Photograph of fabricated circuit board. (b) System block diagram.

that extend around the body. The wingspan is 110 mm. The actuators are composed of single-crystalline Pb(In$_{1/2}$Nb$_{1/2}$)O$_3$-Pb(Mg$_{1/3}$Nb$_{2/3}$)O$_3$-PbTiO$_3$ (PIN-PMN-PT) (manufactured by TRS Technologies. Inc.), which has a large piezoelectric coefficient and is capable of large displacements. The dimensions and geometry of the actuators and wings are the same as those used in a previous study [15]. Glued carbon fiber reinforced polymer (CFRP) rods, 0.28 mm and 0.50 mm in diameter, constitute the body. The electronic circuit and battery were placed at the center of the body, as shown in Fig. 1(a). A small commercial LiPo battery (MW10, MicronWings) was sandwiched between the folded flexible printed circuit (FPC) boards. Eight actuators were driven in pairs, as shown in Fig. 1(b). Therefore, four paired actuators were used. Each paired actuator can flap its wings with an independent amplitude and is designed to stabilize its attitude with quadrotor-like control.

Table I summarizes the mass distribution of the aircraft. The actuator is the heaviest at 928 mg. This is mainly due to the PIN-PMN-PT, which has a high density of approximately 8000 kg/m^3. The combined battery and circuit board weigh 746 mg. The total weight after assembly is 2139 mg.

B. Electronics

Fig. 2(a) shows the fabricated circuit board. The board was manufactured using standard FPC processes. The board is narrower in the center, so that it can be folded; it is divided into upper and lower sections. The upper board contains the processing and

communication circuits. The lower board contains the power conditioning and driver circuits. Fig. 2(b) shows a block diagram of the system. A 3.7 V LiPo battery was used as the power source, and a DC-DC converter circuit capable of outputting up to 175 V generated the high voltage necessary to drive the piezoelectric actuator. A 4-channel high-voltage driver outputs periodic voltage waveforms to make the four paired actuators flap their wings. Signals to the drivers were sent from a microprocessor unit (MPU) (CC2640R2F, Texas Instruments). To drive many actuators using minimal circuitry and MPU ports, we employed flapping amplitude control by digitally controlling the duty ratio of the square-wave driving signals. The board was equipped with
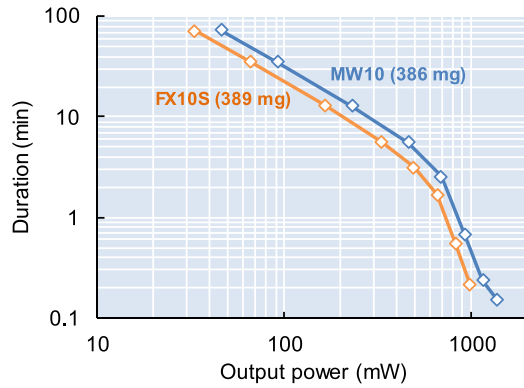
Fig. 3. Typical commercial subgram LiPo battery duration with respect to output power.
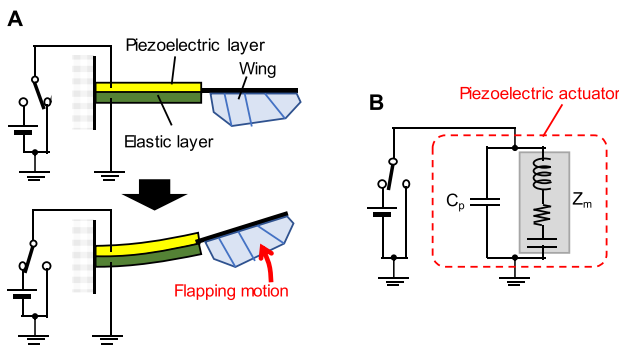

Fig. 4. Behavior of piezoelectric unimorph flapping-wing actuator. (a) Actuation principle. (b) Simplified equivalent circuit.

Fig. 5. Concept of efficiency improvement by HZWM actuation.

a 3-axis magnetic sensor (LIS3MDL, STMicroelectronics) and a 6-axis inertial sensor (LSM6DSM, STMicroelectronics) for attitude estimation, which are necessary for flight stabilization. The MPU is connected to a dipole antenna made of FPC copper patterns, which enables wireless communication via Bluetooth low-energy (BLE).

One of the most important requirements of MAV circuits is low power consumption. For LiPo batteries, as the output power (current) increases, the duration of a LiPo battery decreases proportionally up to a certain point (i.e., the effective capacity is maintained). However, above this power, the duration decreases rapidly. As an example, Fig. 3 shows the output voltage vs. duration curves for two commercially available subgram LiPo batteries (MW10, Micron Wings and FX10S, Indoor Airplane World). In both cases, a sharp decrease in duration was observed, with an inflection point at approximately 600 mW. This is a phenomenon where the effective capacity decreases due to an increase in the internal resistance caused by exceeding the rated power. Therefore, limiting power consumption below this inflection point is desirable.

We designed a low-power circuit specifically for digital duty ratio control. Fig. 4 shows the operation and electrical properties of the piezoelectric actuator. As shown in Fig. 4(a), the piezoelectric unimorph actuator consists of layers of piezoelectric and elastic materials (Ti). When voltage is applied, the actuator deforms in a warping manner. By periodically turning the switch on
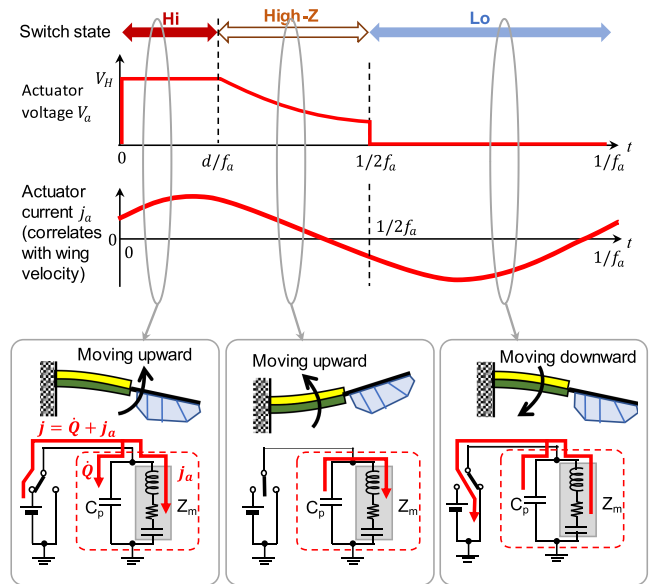
and off with its frequency matching the resonant frequency of the actuator, a large amplitude can be obtained. Piezoelectric actuators can generally be represented as a parallel circuit composed of a parasitic capacitance component C_p and impedance Z_m that represents the mechanical behavior, as shown in Fig. 4(b) [16]. Furthermore, if the mechanical system is linearly approximated, it can be considered as an RLC series circuit where the equation of motion $J\ddot{\phi} + B\dot{\phi} + K\phi = T$ (where J, B, and K are the inertia, damping, and spring constant of the actuator system, respectively) is replaced by the equation of an equivalent electric circuit $L\ddot{Q}_a + R\dot{Q}_a + C^{-1}Q_a = V$. The current flowing in the RLC circuit ($j_a = \dot{Q}_a$) resembles the speed of the actuator ($\dot{\phi}$). The simplest driving method is V_H-ground (GND) switching. However, in this case, the energy $C_pV_H^2$ stored in C_p when V_H is applied is discarded when switching to GND, resulting in a loss. This parasitic capacitance loss is very large and is a key point for improvement.

The proposed circuit incorporates two highly efficient techniques. One is charge recovery by transferring the stored charge of the parasitic capacitor to another actuator. In a previous paper, we reported a passive charge recovery technique using a small number of additional circuit elements [17]; this technique was also employed in the current circuit. The other is a drive technology that provides more lift with the same energy input. This concept is shown in Fig. 5. Generally, pulse-width modulation (PWM) refers to the change in the ratio of the V_H and GND periods. However, we employed high impedance width modulation (HZWM), in which the ratio of the V_H and high impedance periods is changed within a half cycle. First, when a high-voltage V_H is applied, the actuator moves upward. Electrically, the charge flows into C_p and Z_m. Next, when a high impedance is applied, the actuator continues to move upward due to inertia and, electrically, continues to draw a current. At this time, the charge stored in C_p acts as a power source and the
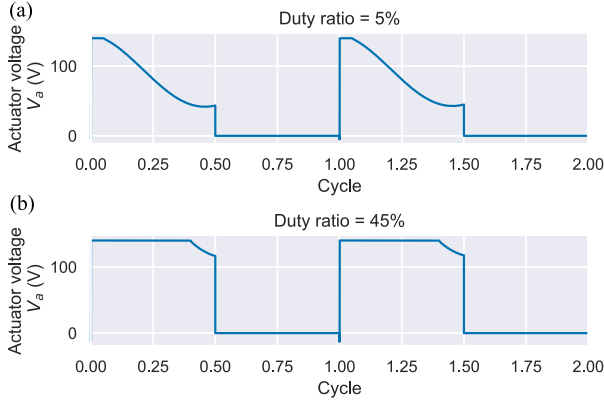
Fig. 6. Simulation result of actuator voltage waveform under HZWM actuation with a duty ratio of (a) 5% and (b) 45%.

actuator is driven by the electrical energy in C_p. Consequently, the potential of the actuator decreases from V_H. At half-cycle, the switch is flipped to GND, and the remaining charge in C_p is discarded. Because the actuator is driven by the stored charge of the parasitic capacitance during the high-impedance period, the flapping amplitude can be increased and the lift-power ratio can be improved.

The efficiency improvement effect of the combination of HZWM drive and charge recovery was confirmed through circuit simulation using LTSpice (Analog Devices Inc.) by replacing the actuator with a simple RLC circuit model. Here, the equivalent circuit parameters of the actuator were obtained by fitting the frequency response characteristics [15]; C_p was 24.4 nF, and the RLC parameters for Z_m were 63.5 kΩ, 607 H, and 3.22 nF, respectively. The switching frequency was set at the 114 Hz resonance frequency of the system, which was experimentally determined from its frequency response (for reference, a simplified theoretical estimation of the resonance frequency is described in Appendix A). Fig. 6(a) and (b) show the waveforms of the actuator voltage V_a when the duty ratio of the high-impedance period is 5% and 45%, respectively.

V_a decreases during the high-impedance period because the charge in C_p flows into Z_m, causing a potential drop, which proves that the system works as designed. Next, we examine how the lift and power consumption change with the use of the HZWM drive. Fig. 7(a) shows a graph comparing the square of the current j_a flowing through Z_m at different duty ratios of the normal PWM drive to HZWM drive. Here, j_a is the speed of the wing. Because the lift is approximately proportional to the square of the stroke velocity, j_a^2 is a parameter that correlates with the lift. As mentioned above, the HZWM drive has a larger j_a^2 than the PWM drive; that is, it is expected to provide increased lift. Fig. 7(b) shows a graph of the duty ratio vs. power consumption P, where the power consumption is also reduced by charge recovery. Fig. 7(c) shows a graph of j_a^2 vs. j_a^2/P; on the horizontal axis, j_a^2 is an index correlated with lift, and j_a^2/P is a value that indicates lift-power efficiency. The HZWM drive showed a 53% average improvement in the j_a^2/P value compared with that of the PWM drive.
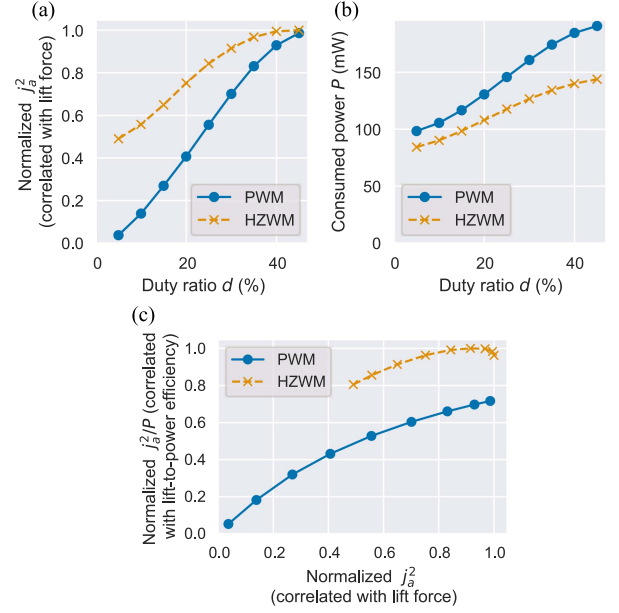

Fig. 7. Simulated actuation performance. (a) Duty ratio – normalized j_a^2. (b) Duty ratio – consumed power. (c) Normalized j_a^2 – normalized j_a^2/P.
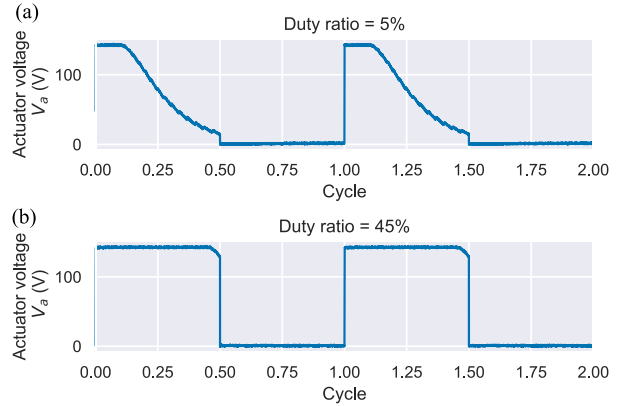

Fig. 8. Measured waveform of actuator voltage under HZWM actuation with a duty ratio of (a) 5% and (b) 45%.

III. RESULTS AND DISCUSSION

A. Actuation Performance

The performance of the actuator was measured using fabricated paired actuators and a prototype drive circuit, with a V_H and frequency f_a of 140 V and 114 Hz, respectively, as in the simulation presented in the previous section (a schematic of the high-voltage driver circuit is shown in Appendix B). Fig. 8 shows the V_a waveforms measured using an oscilloscope. As in the simulation results (Fig. 6), a decrease in V_a was observed during high-impedance periods. Therefore, charge transfer from the parasitic capacitance C_p occurred in the actual device. Fig. 9(a) shows a graph of duty ratio vs. lift force. The lift force was measured by placing the actuator on an electronic balance. In the actual measurement, the HZWM drive could exert a greater lift force than the PWM drive. The power consumption also decreased, as shown in Fig. 9(b), and the lift-power efficiency improved by an average of 93% (Fig. 9(c)).
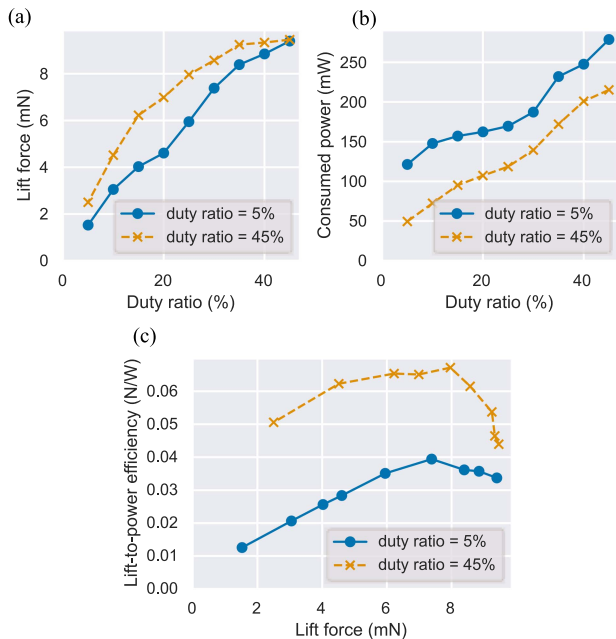
Fig. 9. Measured actuation performance. (a) Duty ratio – lift force. (b) Duty ratio – consumed power. (c) Lift force – lift-to-power efficiency. The lift and power consumption were measured once during duty ratio sweeping.

The power consumption required for flight was estimated from these experimental results. Past studies on larger-scale flapping-wing MAVs have shown aggressive flight where the aircraft have margins of 30-40% of lift relative to their own weight [5], [18]. Therefore, considering a margin of 1.5 times the total mass of the airframe, we defined the target total lift as 31 mN (3.2 gf). This means that the target lift per paired actuator is 7.8 mN. According to Fig. 9, conventional PWM drive achieves a lift force of 7.8 mN at a duty ratio of 32%, whereas HZWM drive achieves a lift force of 7.8 mN at a duty ratio of 24%. The power consumptions of the paired actuators for PWM and HZWM were 208 mW and 110 mW, respectively. Because the boost efficiency of the DC-DC converter in this circuit is approximately 80%, the power required from the battery to drive the four paired actuators is estimated to be 1040 mW and 550 mW for the PWM and HZWM drives, respectively. Based on the battery characteristics shown in Fig. 3, these power consumptions result in a battery duration of approximately 0.4 minutes and 4 minutes, respectively. We measured the durations of the four paired actuators driven by the battery at the duty ratios that produced the target lifting force described above. The results are shown in Fig. 10. The graph shows the time on the horizontal axis and V_H on the vertical axis. The duration for the PWM drive was 0.62 minutes, and that of the HZWM drive was 5.6 minutes. These results are in good agreement with the estimates above. Although the proposed high-efficiency circuit improves the lift-power efficiency of the actuator by approximately a factor of two, a significant improvement by a factor of nine was achieved in the duration because the inflection point, where the battery characteristics deteriorate, is crossed.
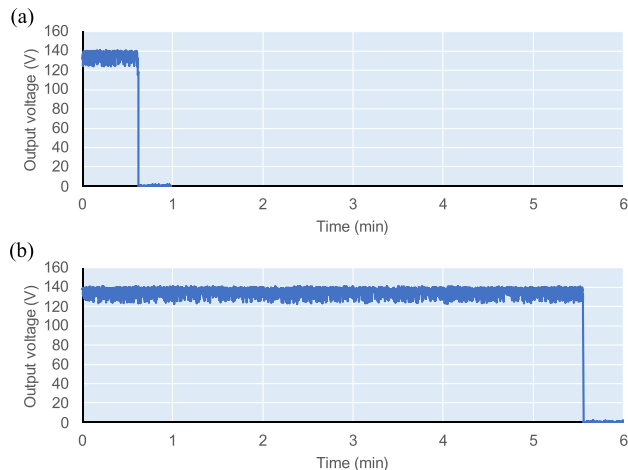

Fig. 10. Output voltage of the DC-DC converter during flapping actuation. (a) PWM actuation. (b) HZWM actuation.
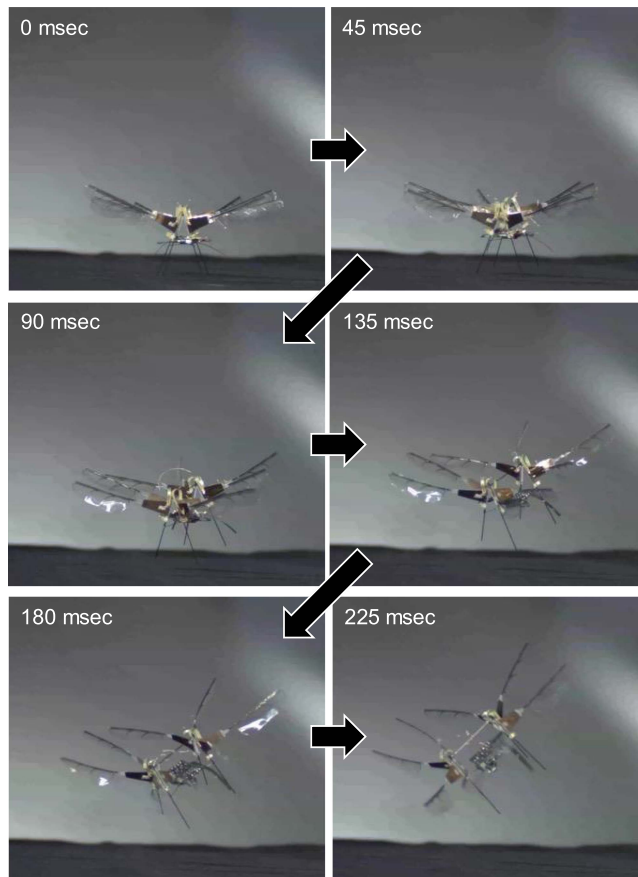

Fig. 11. Untethered take-off demonstration.

B. Take-off Demonstration

We tested an uncontrolled takeoff demonstration using the aircraft. Fig. 11 shows a series of photographs taken from a portion of the takeoff video. The MAV succeeded in taking off in an untethered state, although the aircraft lost balance after takeoff because attitude control was not yet implemented. Here, the command signal to start driving was provided via BLE communication. Because the thrust exerted differs depending

on the performance of the actuators, the drive duty ratios were adjusted individually to make the takeoff as close to vertical as possible. For this trial, the duty ratios were 25%, 20%, 25%, and 27.5% for the right fore, left fore, left rear, and right rear, respectively. The drive voltage and frequency were 140 V and 114 Hz, respectively, as in the previous experiment. Supplementary video material showing three takeoff experiments conducted under the same conditions as in Fig. 11 is available online at https://ieeexplore.ieee.org.

IV. CONCLUSION

We designed and built the first battery-powered, tailless, insect-scale flapping-wing MAV and demonstrated its successful shot-duration takeoff without attitude control. The proposed electronics allowed the aircraft to produce a thrust of 1.5 times its own weight for over 5 min, which is comparable to that of commercially available small drones. We believe that the HZWM control circuitry reported here will contribute not only to flying robots, but also to walking and swimming robots and other micro-robots.

Future work should focus on realizing attitude-controlled flight. Because tethered flight control has already been achieved with an equivalent aircraft (an aircraft with three paired actuators without a circuit board) [19], we believe that attitude-controlled flight based on our MAV design is highly feasible. The first technical point to consider is whether attitude estimation should be performed inside or outside the aircraft. External attitude estimation using optical tracking is more accurate than internal attitude estimation using an inertial measurement unit (IMU). However, the latency of transmitting attitude information via wireless communication may destabilize control. We expect that a combination of attitude estimation using the internal IMU for short time periods and external optical tracking to compensate for long-term drift is a viable strategy. Additionally, installing sensors, such as a camera, is imperative for realizing potential applications. Due to the emergence of mobile application devices (for example, the Sony IU233N2-Z), lightweight camera modules, which weigh a mere 20 mg and consume less than 55 mW, have recently proliferated. As such, installing a camera module is not an arduous task, but processing high-pixel image data may pose challenges, considering the constrained power of the processor and the limited bandwidth for communicating with the external environment.

APPENDIX A: SIMPLIFIED ACTUATOR MODEL

To simplify a flapping actuator as a 1-DoF mechanical system, its resonant frequency f_n can be expressed as follows:

$$f_n = \frac{1}{2\pi} \sqrt{\frac{K_A}{J_W + J_A}}. \tag{A1}$$

where K_A is the spring constant of the actuator, and J_W and J_A are the moments of inertia of the wings and piezoelectric actuator, respectively. As reported in [3], when the deformation of the piezoelectric actuator is approximated as a quadratic
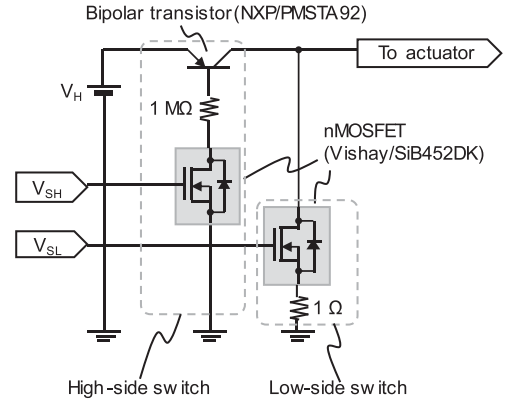

Fig. 12. Schematic of the high-voltage driver.

curve, K_A and J_A, can be expressed as follows:

$$K_A = \kappa \frac{w_r + w_t}{2 L_A}, \tag{A2}$$

$$J_A = \frac{1}{120} \gamma \left(w_r + 5 w_t \right) L_A^3, \tag{A3}$$

where w_r, w_t, and L_A are the tip width, fixed-end width, and length of the piezoelectric actuator, respectively, κ is the bending stiffness of the piezoelectric actuator per unit width, and γ is the area density of the actuator. Approximating the wings as a plate with uniform density, J_W can be expressed as follows:

$$J_W = \frac{1}{12} M_W L_W^2 + M_W \left(\frac{L_W + L_A}{2} \right)^2. \tag{A4}$$

where M_W and L_W are the mass and length of the wing, respectively. Substituting $w_r = 8.5$ mm, $w_t = 4.4$ mm, $L_A = 16.5$ mm, $\kappa = 25.9$ mNm, $\gamma = 1.09$ kg/m^2, $M_W = 17.8$ mg, and $L_W = 36$ mm, the resulting f_n is 128 Hz. The error between the value calculated with this simplified model and the measured value (114 Hz) was 13%.

APPENDIX B: HIGH-VOLTAGE DRIVER CIRCUIT

Fig. 12 shows the circuit diagram of the high-voltage driver circuit. The high-side switch consists of a bipolar transistor in series with an nMOSFET. When the voltage V_{SH} is set to Hi, the nMOSFET on the GND side is closed and current flows to the bipolar transistor, turning it ON. The low-side switch consists of an nMOSFET that can be closed by setting the voltage V_{SL} to Hi.

REFERENCES

[1] R. J. Wood, "Liftoff of a 60mg flapping-wing MAV," in *Proc. IEEE/RSJ Int. Conf. Intell. Robots Syst.*, San Diego, CA, USA, 2007, pp. 1889–1894, doi: 10.1109/IROS.2007.4399502.

[2] K. Y. Ma, P. Chirarattananon, S. B. Fuller, and R. J. Wood, "Controlled flight of a biologically inspired, insect-scale robot," *Science*, vol. 340, no. 6132, pp. 603–607, May 2013, doi: 10.1126/science.1231806.

[3] T. Ozaki and K. Hamaguchi, "Bioinspired flapping-wing robot with direct-driven piezoelectric actuation and its takeoff demonstration," *IEEE Robot. Automat. Lett.*, vol. 3, no. 4, pp. 4217–4224, Oct. 2018, doi: 10.1109/LRA.2018.2863104.

[4] Y. Chen et al., "Controlled flight of a microrobot powered by soft artificial muscles," *Nature*, vol. 575, no. 7782, pp. 324–329, Nov. 2019, doi: 10.1038/s41586-019-1737-7.

[5] M. Karásek, F. T. Muijres, C. De Wagter, B. D. W. Remes, and G. C. H. E. de Croon, "A tailless aerial robotic flapper reveals that flies use torque coupling in rapid banked turns," *Science*, vol. 361, no. 6407, pp. 1089–1094, Sep. 2018, doi: 10.1126/science.aat0350.

[6] S. Tijmons, M. Karásek, and G. de Croon, "Attitude control system for a lightweight flapping wing MAV," *Bioinspiration Biomimetics*, vol. 13, no. 5, Jul. 2018, , Art. no. 056004, doi: 10.1088/1748-3190/aab68c.

[7] H. V. Phan, T. Kang, and H. C. Park, "Design and stable flight of a 21 g insect-like tailless flapping wing micro air vehicle with angular rates feedback control," *Bioinspiration Biomimetics*, vol. 12, no. 3, Apr. 2017, Art. no. 036006, doi: 10.1088/1748-3190/aa65db.

[8] Q.-V. Nguyen, W. L. Chan, and M. Debiasi, "An insect-inspired flapping wing micro air vehicle with double wing clap-fling effects and capability of sustained hovering," *Proc. SPIE*, vol. 9429, pp. 136–146, 2015, doi: 10.1117/12.2085714.

[9] G. C. H. E. de Croon, M. Perçin, B. D. W. Remes, R. Ruijsink, and C. De Wagter, *The DelFly*. Amsterdam, The Netherlands: Springer, 2016 doi: 10.1007/978-94-017-9208-0.

[10] M. H. Rosen, G. le Pivain, R. Sahai, N. T. Jafferis, and R. J. Wood, "Development of a 3.2g untethered flapping-wing platform for flight energetics and control experiments," in *Proc. IEEE Int. Conf. Robot. Automat.*, Stockholm, Sweden, 2016, pp. 3227–3233, doi: 10.1109/ICRA.2016.7487492.

[11] L.-J. Yang, B. Esakki, U. Chandrasekhar, K.-C. Hung, and C.-M. Cheng, "Practical flapping mechanisms for 20 cm-span micro air vehicles," *Int. J. Micro Air Veh.*, vol. 7, no. 2, pp. 181–202, Jun. 2015, doi: 10.1260/1756-8293.7.2.181.

[12] H. V. Phan, Q.-T. Truong, and H.-C. Park, "Implementation of initial passive stability in insect-mimicking flapping-wing micro air vehicle," *Int. J. Intell. Unmanned Syst.*, vol. 3, no. 1, pp. 18–38, Feb. 2015, doi: 10.1108/IJIUS-12-2014-0010.

[13] J. James, V. Iyer, Y. Chukewad, S. Gollakota, and S. B. Fuller, "Liftoff of a 190 mg laser-powered aerial vehicle: The lightest wireless robot to fly," in *Proc. IEEE Int. Conf. Robot. Automat. (ICRA)*, Brisbane, QLD, Australia, 2018, pp. 3587–3594, doi: 10.1109/ICRA.2018.8460582.

[14] N. T. Jafferis, E. F. Helbling, M. Karpelson, and R. J. Wood, "Untethered flight of an insect-sized flapping-wing microscale aerial vehicle," *Nature*, vol. 570, no. 7762, pp. 491–495, Jun. 2019, doi: 10.1038/s41586-019-1322-0.

[15] T. Ozaki, N. Ohta, T. Jimbo, and K. Hamaguchi, "A wireless radiofrequency-powered insect-scale flapping-wing aerial vehicle," *Nature Electron.*, vol. 4, pp. 845–852, Nov. 2021, doi: 10.1038/s41928-021-00669-8.

[16] M. Goldfarb and N. Celanovic, "Modeling piezoelectric stack actuators for control of micromanipulation," *IEEE Control Syst. Mag.*, vol. 17, no. 3, pp. 69–79, Jun. 1997, doi: 10.1109/37.588158.

[17] T. Ozaki and N. Ohta, "Power-efficient driver circuit for piezo electric actuator with passive charge recovery," *Energies*, vol. 13, no. 11, Jun. 2020, Art. no. 2866, doi: 10.3390/en13112866.

[18] Y.-W. Chin et al., "Efficient flapping wing drone arrests high-speed flight using post-stall soaring," *Sci. Robot.*, vol. 5, no. 44, Jul. 2020, Art. no. eaba2386, doi: 10.1126/scirobotics.aba2386.

[19] T. Jimbo, T. Ozaki, Y. Amano, and K. Fujimoto, "Flight control of flapping-wing robot with three paired direct-driven piezoelectric actuators," *IFAC-PapersOnLine*, vol. 53, no. 2, pp. 9391–9398, 2020, doi: 10.1016/j.ifacol.2020.12.2408.